Check for updates

Ultrafast all-optical switching enabled by epsilon-near-zero-tailored absorption in metal-insulator nanocavities

Joel Kuttruff [1], Denis Garoli[2], Jonas Allerbeck [1], Roman Krahne[2], Antonio De Luca[3,4], Daniele Brida [1,5], Vincenzo Caligiuri[2,3,4 ✉] & Nicolò Maccaferri [5 ✉]

Ultrafast control of light—matter interactions is fundamental in view of new technological frontiers of information processing. However, conventional optical elements are either static or feature switching speeds that are extremely low with respect to the time scales at which it is possible to control light. Here, we exploit the artificial epsilon-near-zero (ENZ) modes of a metal-insulator-metal nanocavity to tailor the linear photon absorption of our system and realize a nondegenerate all-optical ultrafast modulation of the reflectance at a specific wavelength. Optical pumping of the system at its high energy ENZ mode leads to a strong redshift of the low energy mode because of the transient increase of the local dielectric function, which leads to a sub-3-ps control of the reflectance at a specific wavelength with a relative modulation depth approaching 120%.

[1] Department of Physics and Center for Applied Photonics, University of Konstanz, 78457 Konstanz, Germany. [2] Istituto Italiano di Tecnologia, 16163 Genova, Italy. [3] Dipartimento di Fisica, Università della Calabria, 87036 Rende, Italy. [4] CNR-Nanotec, 87036 Cosenza, Italy. [5] Department of Physics and Materials Science, University of Luxembourg, 1511 Luxembourg, Luxembourg. ✉email: vincenzo.caligiuri@unical.it; nicolo.maccaferri@uni.lu

Overcoming the fundamental limits of electronics, such as bandwidth, clock-time/frequency and heating of the device, is the main promise of photonics[1]. Many recent advancements in this direction rely on the use of light as information carrier, paving the way towards light-based technologies, which will have a huge impact in terms of reduced energy consumption and performance efficiency. Moreover, the possibility of controlling electronics at optical frequencies has recently become possible, thus introducing a new paradigm towards attosecond opto-electronics[2]. One way to achieve active control of light is represented by electro-optical modulators[3]. Although used in industry[4], they still suffer from limited bandwidth (GHz regime) and large power consumption due to the required electronics. In this framework, it is fundamental to develop new, affordable, and energy-efficient strategies to reach a fast (>100 GHz) and fully tailorable control of optical states at scales which are well below the diffraction limit of electromagnetic radiation. Therefore, all-optical switching[5] has attracted great attention because it can potentially overcome the speed and heat dissipation limitation imposed by electrical switching or passive optical devices[6,7]. In view of practical applications, the key performing parameters of all-optical switching include modulation depth (defined as the reflection and/or transmission contrast between "ON" and "OFF" states) and switching time. The latter defines the bandwidth via the inverse of the transition time between "ON" and "OFF" states[5]. Examples of high-speed all-optical switching devices based on semiconductors[8], photonic[9] and plasmonic[10] crystals,

semiconducting nanostructures[11], metallic[12] and dielectric[13] metasurfaces, single nanoantennas[14] and microring resonators[15] have already been proposed. Another interesting approach is represented by the so-called natural epsilon-near-zero (ENZ) materials[16]. Saha et al.[17] showed that yttrium-doped cadmium oxide (CdO) films can enable light intensity switching with relative modulation depths up to 135% in the mid-infrared (mid-IR) region close to the ENZ point and a switching time of 45.6 ps for a pump fluence of 1.3 mJ cm^{-2}. Moreover, Yang et al.[18] have demonstrated that natural ENZ materials can be used for sub-ps switching. Through intraband optical pumping of an In-doped CdO-based plasmonic perfect absorber, they showed an absolute modulation of light intensity of 85.3% with a switching time of 800 fs and using a pump fluence of 0.34 mJ cm^{-2}. In the case of natural ENZ-based switching however, previous approaches are based on the presence of only one ENZ frequency, the exciting polarization can be only transverse magnetic (TM), and very challenging material processing techniques are required to tailor the ENZ wavelength, for instance by material doping. Recently, it has been found that resonances occurring in metal-insulator-metal (MIM) nanocavities can be described as effective ENZ resonances[19]. Several ENZ points, which can be excited with both TM and transverse electric (TE) polarized light, can be designed at will, and their spectral position can be easily engineered by acting on the refractive index and thickness of the embedded dielectric, while their quality(Q)-factor ($\lambda/\Delta\lambda$) can be optimized by adopting non-symmetric geometries, yielding low reflectance R at the ENZ modes[20,21]. Therefore, these systems constitute a promising and flexible alternative to natural ENZ materials.

Here, we propose an approach for ultrafast all-optical switching based on the perturbation of an artificial ENZ symmetric mode in the near infrared (NIR) through optical pumping of an antisymmetric one in the ultraviolet (UV) region in an MIM nanocavity. The nondegenerate approach we propose here allows a strong modulation of the ultrafast nonlinear response of an ENZ mode via linear absorption of the other ENZ mode we pump by using both TM and TE polarized light. It is worth mentioning here that this concept is general, since the cavity resonances can be designed at will in a broad range of wavelengths (from the UV to mid-IR), and it relies on a simple fabrication process.

Results

Steady-state optical response. The technological core of the architecture is depicted in Fig. 1. At the steady state, both the high-energy (HE) and the low-energy (LE) ENZ modes enable a very high (>90%) photon absorption at the resonances (Fig. 1a). The nanocavity is then used for all-optical switching upon photoexcitation. By optical pumping the HE ENZ mode, the LE resonance strongly redshifts because of the transient increase of the dielectric function upon excitation of charge carriers in the metallic layers[22–24], which leads to a modulation of the reflectance R at the wavelength of the LE mode (Fig. 1b).

To prove the ENZ nature of our system, we first characterized the steady-state spectral response in terms of absolute R as a function of the angle of incidence θ and of the incident light wavelength λ. In Fig. 2 a, b we plot the real (ε', **a**) and imaginary (ε'', **b**) parts of the effective dielectric permittivity, respectively, as measured by ellipsometry, of the sample consisting of an MIM cavity with Ag[30 nm]/Al$_2$O$_3$[180 nm]/Ag[100 nm] layers on top of a glass substrate (more details on the fabrication are reported in the "Methods" section) for $\theta = 30°$ as representative case (for the full angular dependence, see Supplementary Fig. 1). Noticeably, R shows a pronounced suppression around 327, 395 and 730 nm (Fig. 2c), in correspondence to the three zero-crossings of ε', thus confirming their ENZ nature. In particular, the mode occurring at
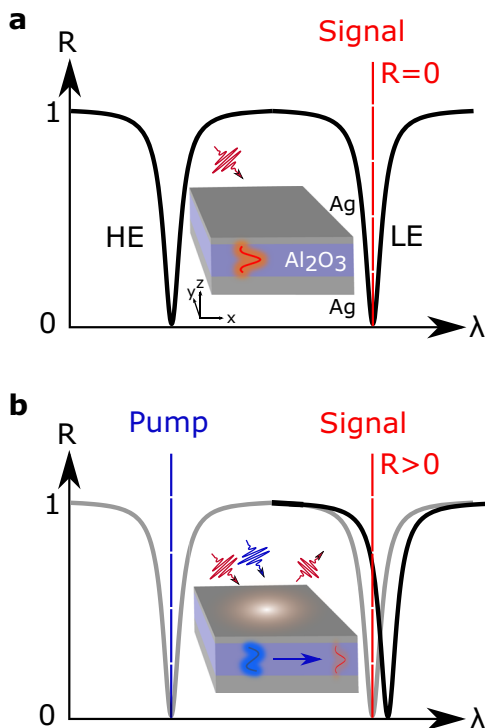

Fig. 1 Ultrafast all-optical switching modulation concept. Sketch of the all-optical switching concept based on a nanocavity supporting two epsilon-near-zero (ENZ) modes. **a** Steady-state reflectance R of a metal-insulator-metal nanocavity: both the high energy (HE) and low energy (LE) resonances display low R at the ENZ points. **b** Upon optical pumping of the HE ENZ mode, the LE absorption resonance redshifts significantly due to a transient increase of the electronic temperature in the metallic building blocks, which leads to a change of R for the signal probe pulse. The equilibrium positions of the resonances are plotted for reference (gray curve).
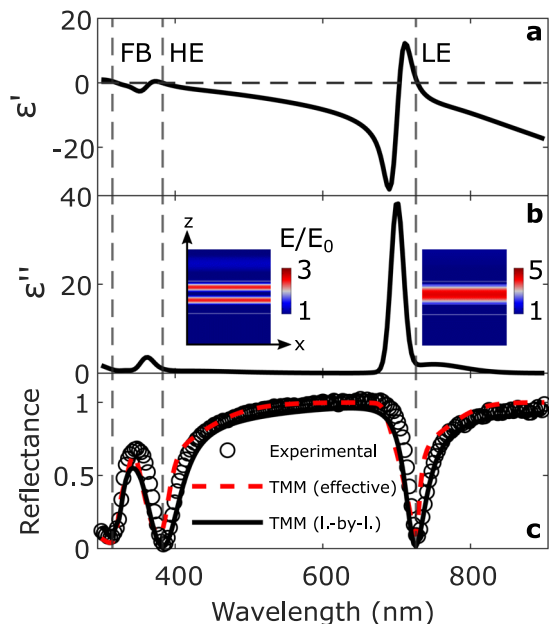
Fig. 2 Steady-state response of the metal-insulator-metal (MIM) nanocavity. Steady-state characterization of the MIM nanocavity made of Ag[30 nm]/Al$_2$O$_3$[180 nm]/Ag[100 nm] layers on a glass substrate as measured at 30° angle of incidence. Real (**a**) and imaginary (**b**) parts of the dielectric permittivity of the MIM nanocavity measured by spectroscopic ellipsometry. The insets in (**b**) show the profiles of the electric field amplitude (color code) of the high-energy (HE) and low-energy (LE) epsilon-near-zero (ENZ) modes normalized to the incoming electric field amplitude E_0 in dependence of spatial coordinates x and z. FB indicates the spectral position of the Ferell−Berreman mode in silver. **c** Experimental (white circles) reflectance compared to transfer matrix method (TMM) calculations carried out by considering a single layer with the measured effective dielectric permittivity (red dashed line) shown in (**a**) and (**b**) and the real (layer-by-layer) structure (black solid curve).

327 nm is the well-known Ferrell−Berreman mode[25–27] (labeled FB), while the ones at ~395 nm (labeled HE) and at ~730 nm (labeled LE) correspond to, respectively, the antibonding and bonding modes of the MIM nanocavity. In the inset of Fig. 2b we also plot the near-field profiles of the two ENZ modes calculated via finite element method simulations (details about the calculations can be found in the "Methods" section). The LE ENZ mode is the symmetric, and the HE ENZ mode is the antisymmetric mode of the MIM cavity[20]. Interestingly, both ENZ modes can be excited with similar efficiency using either TE (s-polarized) or TM (p-polarized) polarization for the incoming light (see also Supplementary Fig. 1), showing that the ENZ resonances represent photonic, rather than plasmonic modes of the cavity. This functionality represents an additional feature if we compare our artificial ENZ nanocavity to natural ENZ media that only support ENZ resonances for p-polarized incident light.

To confirm the validity of the measured effective permittivities, simulations based on the transfer matrix method (TMM) have been performed by considering light impinging at 30° on one homogenized layer with thickness equal to that of the MIM and dielectric permittivity ε' and ε''. The corresponding R (Fig. 2c, red dashed curve) is in excellent agreement with both experiments (Fig. 2c, white circles) and classic layer-by-layer (Fig. 2c, black solid curve) simulations.

All-optical modulation of the nanocavity reflectance. All-optical modulation of the reflectance of the system has been proved by performing wavelength- and time-resolved pump−probe

experiments. The MIM nanocavity was pumped at the HE ENZ mode, while the temporal dynamics were investigated by probing in the 710−770 nm spectral range (Fig. 3a), where the LE ENZ mode is located (more details on the pump and probe signals, as well as on the experimental setup[28], can be found in the "Methods" section, Supplementary Figs. 2 and 3). An incident angle of 30° was chosen for the ultrafast experiments, but our approach can in principle be generalized also to other angles due to the preserved high Q-factor over the angular dispersion of the ENZ modes (see Supplementary Fig. 1). Upon resonant pumping of the HE mode, electrons are photoexcited in the metallic layers, and quickly thermalize via electron−electron and electron-phono scattering, leading to an elevated electronic temperature and thus a transient increase of the local dielectric function[23]. This introduces a redshift of the LE ENZ resonance due to the local increase of permittivity, and thus a pump-induced change $\Delta R/R$ close to the LE resonance. As can be inferred by Fig. 2c, we decided to pump the HE mode since it is the one showing the largest photon absorption (97%). Moreover, the HE mode has also a larger width, so that any tiny shift of this mode is less appreciable compared to the shift of the LE mode which features a higher Q-factor. Therefore, we use the LE mode as the mode we want to modulate the nonlinear response, because it is the one that physically can display the largest variation. We do not exclude that, by pumping directly the LE mode, we might obtain even larger shifts. However, this is against the idea to use the non-degenerate pump−probe scheme we are proposing in this work.

For a pump fluence of ~5.2 mJ cm^{-2}, we indeed observe a positive absolute change of the reflectance ΔR around 10% at the wavelength of the LE ENZ mode, corresponding to a relative modulation $\Delta R/R$ of about 120%, which is our best result so far, and a negative $\Delta R/R$ of about 50% at also in Fig. 3a longer wavelengths (above 735 nm), as it can be seen in Figs. 3b and 4a. The induced reflectance modulations, either positive or negative, are strongly localized at specific wavelengths, and do not shift throughout the relaxation process, at least within the first 5 ps. The absorption of incident light by the metallic layers is drastically enhanced by the presence of the HE mode, thus driving efficient carrier excitation. To validate this concept, we performed off-resonant pumping at 610 nm (see also the "Methods" section and Supplementary Fig. 2 for details), where R is near unity and the absorption is very small (see Fig. 2). Very low $\Delta R/R$ (<0.1%) is observed (see Fig. 4a, gray circles), confirming that the effect is indeed driven by the high absorption at the HE ENZ mode, and that the mutual presence of two ENZ modes is fundamental to achieve such large modulations, when at the same time keeping pump and probe signal pulses spectrally separated.

The physics underlying the dynamics of the nanocavity is dominated by the photoexcitation of charge carriers in the constituent metallic building blocks. In the visible (VIS) and NIR spectral range, the steady-state optical properties of silver can be well described using the Drude model[29],

$$\varepsilon = \varepsilon_{\infty,0} - \frac{\omega_p^2}{\omega(\omega + i\gamma_0)}. \qquad (1)$$

In this model, γ_0 is the damping rate at the equilibrium, and the plasma frequency is given by $\omega_p^2 = \frac{ne^2}{m_{eff}\varepsilon_0}$, where n is the electron density, e the electron charge, m_{eff} the effective electron mass and ε_0 the vacuum permittivity. Contributions to ε from interband transitions of d-band electrons to the sp-band can empirically be accounted for by adding functions of Lorentz oscillators, where the sum is represented in the steady state by $\varepsilon_{\infty,0}$. For $\gamma_0 \ll \omega$, Eq. (2) can be decomposed into contributions to the real ε' and
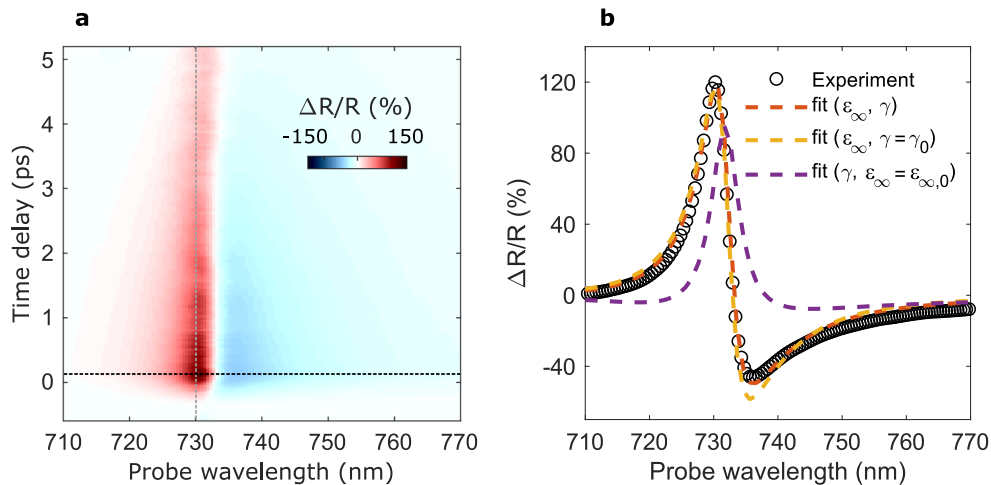
Fig. 3 Ultrafast modulation of the photon reflectance. Time-resolved modulation of the reflectance R at the low-energy (LE) resonance. **a** Time-resolved $\Delta R/R$ pump−probe spectrum in the range 710–770 nm for a pump fluence of 5.2 mJ cm^{-2}. The equilibrium LE epsilon-near-zero (ENZ) mode (vertical dashed line, gray) strongly redshifts upon pumping of the high-energy (HE) ENZ mode, thus enabling a relative modulation of R exceeding 120%. **b** Cut along the spectrum (white circles) shown in (**a**) at 100 fs time delay (horizontal dashed line in (**a**), black). Dashed lines show fits to the data based on multilayer transfer matrix method (TMM) simulations, where the damping γ (violet), the interband term ε_∞ (yellow), or both ε_∞ and γ (orange) of the silver permittivity are changed.

imaginary part ε'' of the permittivity as

$$\varepsilon' = \varepsilon_{\infty,0} - \frac{\omega_p^2}{\omega^2}, \quad \varepsilon'' = \frac{\gamma_0 \omega_p^2}{\omega^3}. \quad (2)$$

The impulsive intraband excitation of electrons in the conduction band initially creates a nonthermal distribution of electrons, which quickly equilibrates mainly via electron−electron and electron−phonon scattering, leading to an elevated electronic temperature accompanied by drastic changes in the interband contribution to ε [22]. More in detail, the hot electron temperature-induced variation of the electronic energy distribution in the conduction band leads to a reduction/increase of the state occupation probability below/above the Fermi energy. That results in a complex modification of the interband transition probability, that can be computed if the band structure of the material is known [30], and leads to a complex behavior of ε_∞ around the interband transition threshold (300 nm in silver) [31]. However, ε_∞ is only weakly dispersive in the spectral range of the LE resonance, i.e. at 730 nm, due to the much higher energy of the interband absorption edge (in this case ε_∞ reduces to a constant contribution to the permittivity). Thus, the transient changes of ε_∞ can be assumed to be almost independent of the wavelength in the spectral region that is probed in this experiment, leading to a constant offset $\Delta\varepsilon_\infty = \varepsilon_\infty - \varepsilon_{\infty,0}$ of the steady-state permittivity. To fit the experimental $\Delta R/R$ spectrum at 100 fs time delay (see Fig. 3b), we use the Drude−Lorentz parameters given by Rakić et al. [32] for silver in the steady state and vary the value of $\Delta\varepsilon_\infty$ in TMM-based simulations. We find a very good agreement with the experimental $\Delta R/R$ data for $\Delta\varepsilon_\infty = 0.5$, indicating that the transient increase of ε_∞ is central for the observed reflectance modulation. Also, changes in the damping γ due to an elevated electronic temperature are considered. By selectively changing ε_∞ and γ in the fit, the dominant role of ε_∞ is further evidenced. When both γ and ε_∞ are varied, we obtain a slightly better fit and observe a transient increase of γ, $\Delta\gamma = \gamma - \gamma_0 = 6$ meV, that can be attributed to an increased electron–electron and electron−phonon coupling for higher electronic temperature. Let us note that this analysis emphasizes the dominant role of an increased ε' for the observed redshift of the LE mode. As can be inferred by

Eq. (2), ε' also changes with the plasma frequency ω_p. Indeed, if small deviations from a perfectly parabolic shape of the conduction band in silver are taken into account, also ω_p changes with the electronic temperature, due to a transient modification of the electron effective mass m_{eff}. Using our simple approach, contributions coming from changes in either ω_p or ε_∞ cannot be fully decoupled. Although it is widely established that changes in ω_p are more related to the lattice temperature [33,34], our quantitative modeling depends strongly on that assumption.

Finally, to evaluate the temporal dynamics and magnitude of the switching process, we fitted the time evolution of $\Delta R/R$ at the position of the LE resonance, i.e. at 730 nm. A single-exponential relaxation model at time delays larger than 200 fs yields the precise decay time of the modulation. Hereby, we also include a constant offset, reflecting dynamics much longer than the temporal window investigated in the experiments. In a second step, we fit a sophisticated model to the complete dynamics between −0.5 and 5 ps based on a Gaussian error function in combination with a double-exponential decay and constant offset, where we fix the slower time constant to the decay time obtained in the first step. From this, we extract the maximum modulation while ensuring the stability of the fit (see Fig. 4a and the "Methods" section).

Performance and limits. The overall performance of our system is characterized by a series of measurements where we varied the excitation pulse fluence from 1.0 up to 7.0 mJ cm^{-2}, shown in Fig. 4. We find an upper working threshold of the device at ~5.2 mJ cm^{-2} (see Fig. 4b).

At high fluence (>5.2 mJ cm^{-2}), we observe a large decrease of $\Delta R/R$ along with irreversible sample damage (see black circles in Fig. 4b and also Supplementary Fig. 4). However, this is not a limiting aspect, since in practical applications lower pulse energies are more relevant than relative modulation depths exceeding 100%, in particular in terms of energy consumption. The relaxation of the system is a complex interplay of several processes triggered by the optical pump that induces a none-quilibrium distribution of the electrons within the metal. The subsequent thermalization of hot electrons with the lattice is the dominant relaxation mechanism [22]. Additional scattering with
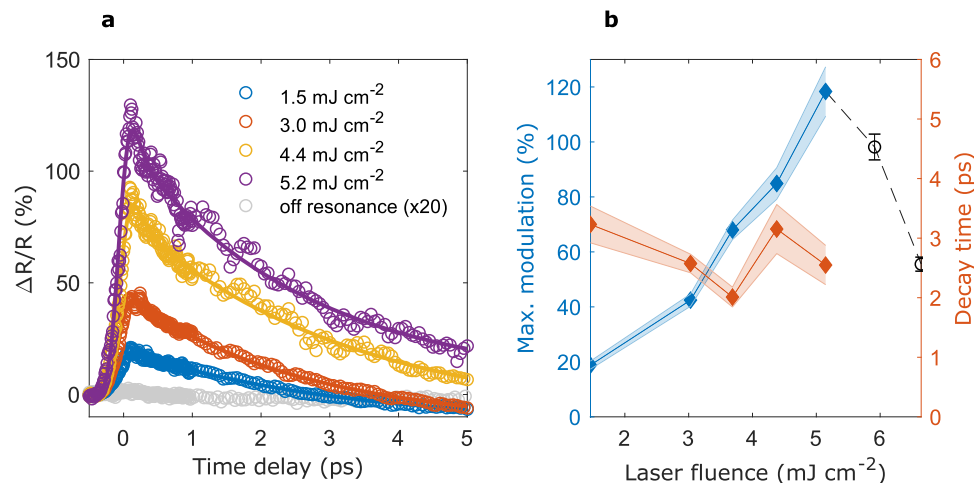
Fig. 4 Performances and limits of the nanocavity-based all-optical switching. Switching performance of our device for different pump pulse fluences. **a** Time-dependent $\Delta R/R$ at probe wavelength $\lambda = 730$ nm for increasing excitation pulse fluences from 1.5 mJ cm^{-2} up to 5.2 mJ cm^{-2}. The gray circles correspond to off-resonant pumping at $\lambda = 610$ nm with pump fluence of 3.3 mJ cm^{-2}. Solid lines show a double-exponential fit model as described in the "Methods" section. **b** Maximum modulation and decay time as a function of pump pulse fluence. Maximum modulation was extracted from a double-exponential fit, while the decay time was obtained by a single-exponential fit considering only time delays larger than 200 fs. Shaded areas indicate the fit uncertainty. Below ≈ 5.5 mJ cm^{-2} (blue diamonds), we find ultrafast switching behavior, yielding outstanding modulation of about 120% at 5.2 mJ cm^{-2}. At higher fluence (black circles), the signal modulation decreases rapidly due to irreversible sample damage. The decay time does not change substantially and remains around 3 ps for all measurements.

acoustic phonons and heat diffusion within the metallic films[24] also influence the time scales observed in the experiments. The overall measured relaxation time will thus be determined by the time scales, relative contributions and the interplay of these mechanisms, which all depend on the excitation fluence. However, as can be seen in Fig. 4b, the decay time remains approximately 3 ps in the range of investigated fluences. For a pump fluence of 5.2 mJ cm^{-2}, we find a decay time of (2.5 ± 0.3) ps corresponding to an all-optical switching bandwidth of about 400 GHz with a relative modulation depth of about 120%. In our case, the switching time is intrinsically limited to the ps time scale by the carrier density and electron heat capacity of the metals that are used. The bottleneck of the device is thus the switching time rather than the spectral bandwidth (>10 nm) of operation, which is dictated by the Q-factor of the ENZ modes. In principle, to overcome this limitation, by combining layers of transparent conducting oxides (TCOs) and dielectrics, the device would benefit from the lower carrier density and electron heat capacity of TCOs as compared to the noble metals[35]. This would translate to a faster electron−phonon coupling and thus enable even higher switching speeds of the cavity. Moreover, the MIM nanocavity can be engineered to work at a desired wavelength, from UV to mid-IR, with practically no limitation regarding the materials involved, and the free spectral range between the ENZ resonances can be easily engineered by exploiting multiple cavity geometries, without affecting the Q-factor of the resonances[21].

Finally, it is worth mentioning here another interesting effect observed in our experiments. After the initial electronic relaxation (time delays > 5 ps), oscillations of $\Delta R/R$ on the order of 10% can be observed within the time-delay range we can explore in our experiments (see Supplementary Fig. 5a). After arrival of the pump pulse, part of the optical energy is converted into mechanical energy due to photoinduced thermal stress. This leads to the formation of acoustic shockwaves and thus a transient opto-acoustic modification of the sample reflectance. In more detail, after Fourier analysis of the signal at the wavelength of the LE mode, fast (~60 GHz) and slow (~10 GHz) oscillations can be distinguished, corresponding to the propagation of acoustic shockwaves in the metal and dielectric layers

respectively. The induced modulations then damp away in a few hundred ps via attenuation of the optically triggered acoustic shockwaves (see also Supplementary Fig. 5b). Although these results go beyond the scope of the current work, we do not exclude the possibility that by engineering the acoustic response of our cavity, namely by creating a hybrid opto-acoustic cavity, we could match the oscillation frequency of an acoustic mode of the cavity in the GHz range, thus potentially enhancing the opto-acoustic modulation of the nonlinear optical response of our system beyond the observed 10%. This additional functionality might be then further exploited in a multifunctional device that combines optical and acousto-mechanical properties, which can be eventually modulated by using external agents such as magnetic fields or spin currents if the metallic layers are made of a magnetic material[36,37].

Discussion

We have demonstrated all-optical, ultrafast (sub-3-ps) switching of the reflectance of a metal−insulator−metal nanocavity approaching a relative modulation depth of 120% in the VIS-NIR spectral range. Our approach is based on the high absorbance of the nanocavity ENZ modes, whose spectral position can easily be tailored at will from UV to mid-IR frequencies, thus lifting from demanding fabrication processes to tailor the spectral position of the ENZ resonance. Via pumping of one ENZ mode, we achieve a relative modulation of reflectance at wavelengths close to the other mode. Without the need of driving higher order effects for ultrafast switching, our system is based on linear absorption, providing large relative modulation exceeding 100% and switching bandwidths of few hundred GHz at moderate excitation fluence, due to the high Q-factor of the ENZ modes. The nondegenerate operation then allows easy separation of pump and signal light via spectral filtering, which is critical in terms of input/output isolation in optical logic applications[38]. Moreover, the proposed system can work with both TE and TM polarization, which is not the case for natural ENZ materials. When combined with other photonic devices, the proposed system can thus be used for ultrafast control of arbitrarily designed

electromagnetic fields. This flexibility is especially valuable when integrating this system with architectures that possess a well-defined dipole moment, such as 2D materials[39], plasmonic nanostructures[40] or single emitters[41]. Our approach proves that we can design at will a tailorable pumping channel and thus a tunable probe signal modulation, which is not easily achievable in natural ENZ materials, where only doping can shift the ENZ point. Furthermore, the primary benefits of this system are that (i) it is easy to fabricate and (ii) its widely tunable optical response lays on the simple fact that the spectral positions of the ENZ resonances depend on the geometry of the nanocavity, while its limitations in terms of switching time and Q-factor depend on the materials that are used, which are well established and readily available.

Finally, we foresee that this approach can also be used as platform for the ultrafast manipulation of optical nonlinearities, such as second and third harmonic generation, Purcell factor enhancement and other very promising future and emerging light-driven technologies.

Methods

Fabrication. Metal−insulator−metal samples have been prepared by electron beam evaporation in a custom-made vacuum chamber at the base pressure of 1×10^{-6} mbar. Ag and Al_2O_3 layers have been deposited at 0.2 and 0.4 Å s^{-1}, respectively. The layer thicknesses have been measured by quartz microbalance.

Optical characterization. Steady-state optical response of the samples has been recorded with a V-VASE J.A. Woollam spectroscopic ellipsometer. Spectroscopic ellipsometry supplied with p- and s-polarized transmittance and reflectance in the spectral range between 300 and 1300 nm was performed to measure the ellipsometric angles ψ and Δ, whose fitting led to the effective permittivity of the sample. Reflectance and transmittance measurements with p- and s-polarization were performed in the angular range from 30° to 80°.

Pump−probe experiments. Transient reflection measurements are carried out with a home-built spectroscopy system based on a commercial Yb:KGW regenerative amplifier system at a laser repetition rate of 50 kHz [28]. A noncollinear optical parametric amplifier (NOPA) working in the VIS/NIR spectral range initially delivers bandwidth-limited pulses at 790 nm that are frequency-doubled using a BBO crystal yielding the final pump pulses with 1.8 nm spectral bandwidth (FWHM) centered at 395 nm (Fourier limit of pulses ~130 fs). Residual spectral components at lower energy are suppressed with a dielectric short-pass filter (Thorlabs, FESH500). For the off-resonant pumping experiments, another NOPA working in the VIS is used, where a 610 nm band-pass filter (Edmund Optics) is put before the parametric amplification, yielding final pump pulses with 8 nm spectral bandwidth centered at 610 nm (Fourier limit of pulses ~70 fs). The pump-induced change of reflection is probed by a white-light supercontinuum between 500 and 900 nm which is temporally compressed by custom-designed dielectric chirped mirrors. The probe pulse energy is then adjusted to ensure a 1:20 energy ratio compared to the pump. Using an off-axis parabolic mirror with 50.8 mm focal length, focal diameters of 20 and 25 μm are achieved for probe and pump pulses, respectively. Pump and probe pulses are focused onto the sample noncollinearly, in order to spatially block the pump pulse after sample interaction. Residual scattered pump radiation is further spectrally suppressed with a dielectric long-pass filter (Thorlabs, FELH600). Spectrally resolved detection of the probe pulse after sample interaction is achieved by using a spectrograph (Acton) in combination with a high-speed charge coupled device camera operating at 50 kHz. Finally, a Pockels cell modulates the pump pulse train at half the repetition rate of the laser system, allowing the calculation of $\Delta R/R$ on a 25 kHz basis.

Two-step fit model. To extract the decay time of the modulation, the following model 1 was used.
1. Model decay time τ: $M(t) = A \cdot \exp\left(-\frac{t-t_0}{\tau}\right) + C$ (for $t > 0.2$ ps)
The amplitude of the modulation is found as the maximum of the following model 2, that describes the complete dynamics from −0.5 ps to 5 ps. The time constant τ is fixed in this model and taken from model 1.
2. Model amplitude with fixed
τ: $M(t) = \frac{1}{2}\left[\text{erf}\left(\frac{t-t_0}{\sigma}\right) + 1\right] \cdot \left[B_{\text{fast}}\exp\left(-\frac{t-t_0}{\tau_{\text{fast}}}\right) + B\exp\left(-\frac{t-t_0}{\tau}\right) + C_0\right].$

Simulations. Numerical simulations were performed with the finite elements method using the commercial COMSOL Multiphysics software. The geometry was set up in 2D, and periodic boundary conditions with Floquet-periodicity were used for the simulation. Linearly polarized light (plane wave), either with p- or s-polarization, at different wavelengths was generated via periodic ports at the top of the simulation geometry. Interpolated data from Rakić et al.[32] and from Boidin et al.[42] were used to describe the linear optical properties of the silver and alumina layers, respectively. Transfer matrix method-based simulations have been carried out via a custom MatLAB code based on the classic formulation that can be found in ref.[43].

References
1. International roadmap for devices and systems. https://irds.ieee.org/roadmap-2017 (IEEE, 2017).
2. Ludwig, M. et al. Sub-femtosecond electron transport in a nanoscale gap. *Nat. Phys.* **16**, 341–345 (2020).
3. Reed, G. T., Mashanovich, G., Gardes, F. Y. & Thomson, D. J. Silicon optical modulators. *Nat. Photon.* **4**, 518–526 (2010).
4. Smit, M. et al. An introduction to InP-based generic integration technology. *Semicond. Sci. Technol.* **29**, 083001 (2014).
5. Chai, Z. et al. Ultrafast all-optical switching. *Adv. Optical Mater.* **5**, 1600665 (2017).
6. Bergman, K., Shalf, J. & Hausken, T. Optical interconnects and extreme computing. *Opt. Photonics N.* **27**, 32–39 (2016).
7. Werner, S., Navaridas, J. & Luján, M. A survey on optical network-on-chip architectures. *ACM Comput. Surv.* **50**, 1–37 (2017).
8. Grinblat, G. et al. Ultrafast sub–30-fs all-optical switching based on gallium phosphide. *Sci. Adv.* **5**, eaaw3262 (2019).
9. Nozaki, K. et al. Sub-femtojoule all-optical switching using a photonic-crystal nanocavity. *Nat. Photon.* **4**, 477–483 (2010).
10. Pohl, M. et al. Plasmonic crystals for ultrafast nanophotonics: optical switching of surface plasmon polaritons. *Phys. Rev. B* **85**, 081401(R) (2012).
11. Fischer, M. P. et al. Optical activation of germanium plasmonic antennas in the mid-infrared. *Phys. Rev. Lett.* **117**, 047401 (2016).
12. Ren, M. et al. Nanostructured plasmonic medium for terahertz bandwidth all-optical switching. *Adv. Mat.* **23**, 5540–5544 (2011).
13. Shcherbakov, M. R. et al. Ultrafast all-optical tuning of direct-gap semiconductor metasurfaces. *Nat. Commun.* **8**, 17 (2017).
14. Grinblat, G. et al. Sub-20 fs all-optical switching in a single Au-Clad Si nanodisk. *Nano Lett.* **18**, 7896–7900 (2018).
15. Pelc, J. S. et al. Picosecond all-optical switching in hydrogenated amorphous silicon microring resonators. *Opt. Express* **22**, 3797–3810 (2014).
16. Kinsey, N. et al. Epsilon-near-zero Al-doped ZnO for ultrafast switching at telecom wavelengths. *Optica* **2**, 616–622 (2015).
17. Saha, S. et al. Broadband, high-speed, and large-amplitude dynamic optical switching with yttrium-doped cadmium oxide. *Adv. Funct. Mater.* **30**, 1908377 (2019).
18. Yang, Y. et al. Femtosecond optical polarization switching using a cadmium oxide-based perfect absorber. *Nat. Photon.* **11**, 390–395 (2017).
19. Caligiuri, V., Palei, M., Imran, M., Manna, L. & Krahne, R. Planar double-epsilon-near-zero cavities for spontaneous emission and Purcell effect enhancement. *ACS Photon.* **5**, 2287–2294 (2018).
20. Caligiuri, V., Palei, M., Biffi, G., Artyukhin, S. & Krahne, R. A semi-classical view on epsilon-near-zero resonant tunneling modes in metal/insulator/metal nanocavities. *Nano Lett.* **19**, 3151–3160 (2019).
21. Caligiuri, V., Palei, M., Biffi, G. & Krahne, R. Hybridization of epsilon-near-zero modes via resonant tunneling in layered metal-insulator double nanocavities. *Nanophotonics* **8**, 1505–1512 (2019).
22. Della Valle, G., Conforti, M., Longhi, S., Cerullo, G. & Brida, D. Real-time optical mapping of the dynamics of nonthermal electrons in thin gold films. *Phys. Rev. B* **86**, 155139 (2012).
23. Del Fatti, N. et al. Nonequilibrium electron dynamics in noble metals. *Phys. Rev. B* **61**, 16956 (2000).
24. Hohlfeld, J. et al. Electron and lattice dynamics following optical excitation of metals. *Chem. Phys.* **251**, 237–258 (2000).
25. Ferrell, R. A. & Stern, E. A. Plasma resonance in the electrodynamics of metal films. *Am. J. Phys.* **30**, 810–812 (1962).
26. Ferrell, R. A. Predicted radiation of plasma oscillations in metal films. *Phys. Rev.* **111**, 1214–1222 (1958).

27. Berreman, D. W. Infrared absorption at longitudinal optic frequency in cubic crystal films. *Phys. Rev.* **130**, 2193–2198 (1963).
28. Grupp, A. et al. Broadly tunable ultrafast pump-probe system operating at multi-kHz repetition rate. *J. Opt.* **20**, 014005 (2017).
29. Marković, M. I. & Rakić, A. D. Determination of optical properties of aluminium including electron reradiation in the Lorentz-Drude model. *Opt. Laser Technol.* **22**, 394–398 (1990).
30. Rosei, R. Temperature modulation of the optical transitions involving the Fermi surface in Ag: theory. *Phys. Rev. B* **10**, 474–483 (1970).
31. Bigot, J., Halté, V., Merle, J. & Daunois, A. Electron dynamics in metallic nanoparticles. *Chem. Phys.* **251**, 181–203 (2000).
32. Rakić, A., Djurišić, A., Elazar, J. & Majewski, M. Optical properties of metallic films for vertical-cavity optoelectronic devices. *Appl. Opt.* **37**, 5271 (1998).
33. Owens, D. T., Fuentes-Hernandez, C., Hales, J. M., Perry, J. W. & Kippelen, B. A comprehensive analysis of the contributions to the nonlinear optical properties of thin Ag films. *J. Appl. Phys.* **107**, 123114 (2010).
34. Baida, H. et al. Ultrafast nonlinear optical response of a single gold nanorod near its surface plasmon resonance. *Phys. Rev. Lett.* **107**, 057402 (2011).
35. Traviss, D., Bruck, R., Mills, B., Abb, M. & Muskens, O. Ultrafast plasmonics using transparent conductive oxide hybrids in the epsilon-near-zero regime. *Appl. Phys. Lett.* **102**, 121112 (2013).
36. Temnov, V. V. Ultrafast acousto-magneto-plasmonics. *Nat. Photon.* **6**, 728–736 (2012).
37. Razdolski, I. et al. Nanoscale interface confinement of ultrafast spin transfer torque driving non-uniform spin dynamics. *Nat. Commun.* **8**, 15007 (2017).
38. Miller, D. A. Are optical transistors the logical next step? *Nat. Photon.* **4**, 3–5 (2010).
39. Brotons-Gisbert, M. et al. Engineering light emission of two-dimensional materials in both the weak and strong coupling regimes. *Nanophotonics* **7**, 253–267 (2018).
40. Mignuzzi, S. et al. Nanoscale design of the local density of optical states. *Nano Lett.* **19**, 1613–1617 (2019).
41. Caligiuri, V. et al. Angle and polarization selective spontaneous emission in dye-doped metal/insulator/metal nanocavities. *Adv. Opt. Mater.* **8**, 1901215 (2020).
42. Boidin, R., Halenkovič, T., Nazabal, V., Beneš, L. & Němec, P. Pulsed laser deposited alumina thin films. *Ceram. Int.* **42**, 1177–1182 (2016).
43. Born, M. & Wolf, E. *Principles of Optics* (Pergamon Press, Oxford, 1970).

Author contributions

J.K., V.C. and N.M. conceived and developed the concept. J.K. and J.A. performed the time-resolved pump−probe experiments. V.C. designed the structure with inputs from J.K. and N.M., and D.G. and R.K. fabricated the samples and characterized the steady-state optical response. V.C. and A.D.L. performed numerical simulations and semi-analytical description of the steady-state epsilon-near-zero behavior of the nanocavity. J.K. developed the model describing the ultrafast dynamics. J.K., D.B. and N.M. analyzed the data. N.M. supervised the work. All the authors participated in the discussion and in the manuscript preparation.

Competing interests

The authors declare no competing interests.

Additional information

Supplementary information is available for this paper at https://doi.org/10.1038/s42005-020-0379-2.

Correspondence and requests for materials should be addressed to V.C. or N.M.

Reprints and permission information is available at http://www.nature.com/reprints

Publisher's note Springer Nature remains neutral with regard to jurisdictional claims in published maps and institutional affiliations.